Applied Physics A (2024) 130:383
https://doi.org/10.1007/s00339-024-07559-8

Applied Physics A
Materials Science & Processing

Transient reflectance of silicon carbide during laser-induced phase separation

Theo Pflug[1] · Benjamin Bernard[2] · Falko Jahn[1] · Michael Gobald[2] · Steffen Weißmantel[1] · Alexander Horn[1]

Received: 14 February 2024 / Accepted: 29 April 2024

Abstract
Laser irradiation can induce local modulations of functional material properties, such as a decreased resistivity or a variation in reflectance. Recent studies investigated the laser-induced phase separation of 4 H-SiC into carbon and silicon on top of regrown SiC to customize its electrical conductivity for the application in electronic devices. To understand the physical processes leading to the laser-induced phase separation, time-resolved pump-probe measurements represent a suitable tool. This study advances the state of the art by characterizing the transient reflectance changes in 4 H-SiC upon irradiation by spatially resolved pump-probe reflectometry. Since the laser heating alters the reflectance of the sample, the spatially resolved measurement enables to observe the heat conduction from the irradiated to the non-irradiated areas, which sustains for several milliseconds. Numerical simulations of the temperature evolution reveal a restricted one-dimensional heat conduction into depth due to the broad lateral extent of the irradiated area. The associated sustained increased temperature within the irradiated area most certainly abets the feasibility of the phase separation. These findings offer practical insights for optimizing the applied laser parameters to tailor the material properties via phase separation.

Keywords Silicon carbide · Excimer laser · Imaging pump-probe reflectometry · Transient reflectance · Phase separation

1 Introduction

Laser radiation is increasingly utilized to precisely tailor and customize the geometrical as well as the functional properties of a material. Laser annealing below the ablation threshold fluence allows to change the optical and electrical properties of thin films used e.g. in photovoltaics [1–6]. Recent studies investigated the laser-induced phase separation of 4 H-SiC into thin Si and C layers in order to tune the electrical conductivity for the application in electronic devices [7, 8]. However, despite consistently yielding separate Si and C layers on top of a regrown SiC area, their reported atomic structures slightly differ in the literature. High-resolution transmission electron microscopy (HR-TEM) revealed either a regrown 3C-SiC layer [7] or individual grains consisting of 3C-SiC and 6 H-SiC [8] on top of the pristine 4 H-SiC after irradiation. On top of this regrown SiC layer is either a crystalline or polycrystalline Si film located. The uppermost C layer tends to be predominantly amorphous but exhibits partial graphitic layers. A similar phenomenon of phase separation has also been reported for 6 H-SiC [9], where approximately 10 regrown lattice planes were observable on top of the pristine SiC by HR-TEM, which have been attributed to multilayers of graphene. To comprehensively understand the underlying physical processes leading to the desired laser-induced material properties, time-resolved pump-probe measurements represent an established method to observe the transient dynamics during and after laser heating [7, 10–14]. Specifically, time-resolved reflectometry measurements, although lacking a spatial resolution, revealed an increased reflectance of 4 H-SiC after excimer laser irradiation that persists for a few hundred nanoseconds, and is assigned to a transiently molten state [7].

In order to extend the state of the art, this study investigates the transient reflectance of SiC upon excimer laser irradiation by spatially resolved pump-probe reflectometry [10, 15, 16]. The spatial resolution of the pump-probe reflectometry not only allows the determination of the transient reflectance during the phase separation process, but also

✉ Theo Pflug
pflug@hs-mittweida.de

[1] Laserinstitut Hochschule Mittweida, Hochschule Mittweida, Technikumplatz 17, Mittweida 09648, Germany

[2] Ion Implantation, Infineon Technologies, Siemensstraße 2, Villach 9500, Austria

Published online: 08 May 2024

enables to characterize the heat affected zone broadening over time due to heat conduction. In addition to the excimer laser irradiation via mask projection, the SiC wafer has also been irradiated with focused laser radiation. In comparison, the area being irradiated by mask projection is three orders of magnitude larger than the area irradiated by the focused radiation. Eventually, while the large-area irradiation via mask projection enables laser-induced phase separation, no such effect was achievable by using focused irradiation. Reasons for that might be the much higher absorption coefficient of the excimer laser radiation and the constrained one-dimensional heat conduction due to the much larger area being irradiated by mask projection. Consequently, the area irradiated using mask projection features a slower cooling rate being favorable to achieve the laser-induced phase separation. This assumption is supported by two-dimensional simulations of the temporal temperature evolution.

The findings presented here provide insights for optimizing the fluence, beam dimensions, and pulse duration of the laser radiation applied to induce phase separation in SiC. These optimizations allow for tailoring the electrical properties of SiC.

2 Materials and methods

2.1 Sample characterization

The investigated sample is a nitrogen-doped n-type 4 H-SiC wafer with a thickness of $d = 350$ µm and a resistivity of 15 mΩcm. The wafer exhibits on-axis (0001) orientation. The refractive index of 4 H-SiC for the wavelength 532 nm has been determined to $n(532\ \text{nm}) = 2.67$ using a commercial imaging ellipsometer (nanofilm_ep4, Accurion) resulting in a reflectivity of $R(532\ \text{nm}) = 0.21$ at the air-SiC interface for an angle of incidence of $\theta = 0°$. The surface roughness $R_a = 7.8$ nm has been determined according to DIN EN ISO 4287:2010 based on the topography measured by laser scanning microscopy, as demonstrated in Sect. 3.1.

In order to investigate the laser-induced phase separation in the SiC sample after irradiation, a focused ion beam (FIB) was used to cleave and smooth a cross-section of the irradiated area. Rough ion beam polish at 30 kV and beam current of 4 nA followed by a finer 30 kV and 150 pA polish has been used. A platinum layer was deposited on top of the SiC sample for sample surface protection. Transmission electron microscopy experiments were carried out using a FEI Tecnai F20 Transmission Electron Microscope with a 200 kV field emission gun.

2.2 Sample irradiation

The 4 H-SiC wafer was irradiated on the one hand with mask-projected and on the other with focused laser radiation.

For mask projection, a krypton fluoride excimer laser (LPX 305F, Coherent, wavelength $\lambda_{pump} = 248$ nm, pulse duration $\tau_{H,pump} = 30$ ns) was used. The excimer laser radiation was projected onto the sample surface by using a photo mask and an objective (focal length 85 mm), resulting in a homogeneous flat top intensity distribution with the lateral dimensions of $1 \times 1\ \text{mm}^2$ (Fig. 1a + b), resulting in an irradiated area of $A_{mask} = 10^{-6}\ \text{m}^2$.

In the case of focused irradiation, a solid state laser (Q1B-10-1064-TH, Quantum Light Instruments, wavelength $\lambda_{pump} = 355$ nm, pulse duration $\tau_{H,pump} = 2.7$ ns) has been applied. The laser radiation was focused onto the SiC surface by a focusing lens (focal length 150 mm) resulting in a beam radius of $w_{86} \approx 17$ µm (Fig. 1c + d). Therefore, the irradiated area $A_{focus} \approx 10^{-9}\ \text{m}^2$ was approximately three orders of magnitude smaller than the area A_{mask} irradiated by excimer laser radiation. The beam radius w_{86} of the raw beam is specified to 0.75 mm at a distance of 20 cm from the laser output. The beam radius of the focused laser radiation on the sample surface has been

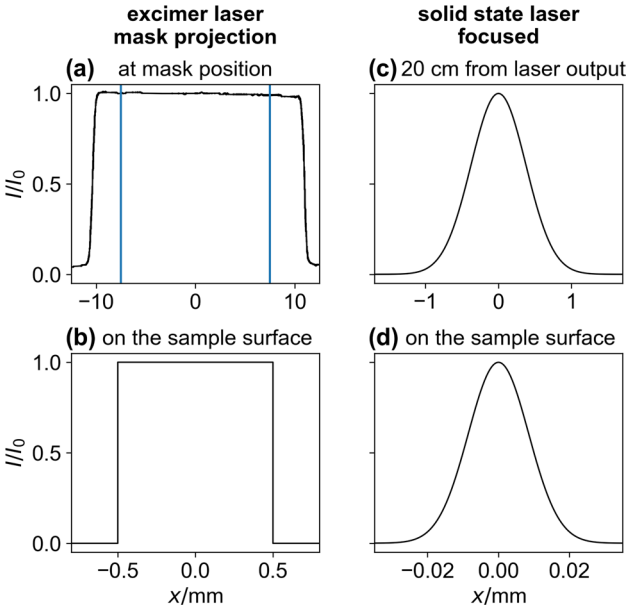

Fig. 1 Measured spatial intensity distribution of the excimer laser radiation at the position of the photo mask (**a**) and the schematic spatial intensity distributions of the excimer laser radiation on the sample surface (**b**), the solid state laser radiation before the focusing lens (**c**), and the focused solid state laser radiation on the sample surface (**d**). The dimensions of the photo mask are indicated by the blue lines in (**a**)

estimated theoretically by considering a Gaussian spatial intensity distribution and the specified beam divergence of 2 mrad [17].

2.3 Pump-probe setup

The pump-probe method applies high-intensity pump radiation to excite a sample material, and probe radiation that interacts with the excited material, whose transient optical properties then deviate from those at room temperature (Fig. 2a).

In this work, the pump radiation is generated by the krypton fluoride excimer laser (LPX 305F, Coherent, wavelength λ_{pump}= 248 nm, pulse duration $\tau_{\mathrm{H,pump}}$= 30 ns) introduced in the previous Sect. 2.2, whereas the probe radiation is emitted by a solid state laser (Explorer XP 532, Spectra-Physics, wavelength λ_{probe}= 532 nm, pulse duration $\tau_{\mathrm{H,probe}}$= 5 ns). Both pump and probe radiation are temporally synchronized relatively to each other by an external delay generator, resulting in a maximum temporal delay of t_{max}= 1 ms with a minimum step width of Δt= 1 ns.

The probe radiation is guided through the objective onto the sample surface. The illuminated sample surface is then imaged onto the CCD chip (1280 × 1024, pixel size 4.8 × 4.8 µ m^2, 10 bit) by the same objective. In front of the upper beam splitter, a lens with a focal length of 100 mm enables the adjustment of the size of the probe radiation spot on the sample surface to homogeneously illuminate the CCD chip. A bandpass filter (center wavelength 550 nm, FWHM bandwidth 40 nm) in front of the CCD chip prevents the detection of the reflected pump radiation. The area of the irradiated sample surface imaged onto the CCD chip is schematically demonstrated in Fig. 2b. Since the 4 H-SiC sample is transparent for the probe radiation at the wavelength 532 nm [18], the incident probe radiation is partially reflected on the top and the rear side of the sample (Fig. 2c). Therefore, the detected signal on the CCD chip is given by $R \propto \left(E_1 + E_2\right)^2$, with the electric field strength of the probe radiation being reflected on the top (E_1) and the rear (E_2) interface of the sample.

In order to measure the relative change of reflectance $\Delta R/R$ of the sample upon irradiation with single pulsed laser radiation, the radiation reflected on the sample surface $R_0(x, y)$ before irradiation and the radiation reflected on the irradiated sample surface $R_{\mathrm{i}}(x, y, t)$ at different delay times t are measured separately (Fig. 3). The spatially and temporally resolved relative change of reflectance $\Delta R/R(x, y, t)$ is then calculated by

$$\Delta R/R(x, y, t) = \frac{R_{\mathrm{i}}(x, y, t) - R_0(x, y)}{R_0(x, y)} \quad . \tag{1}$$

The interference patterns being visible in Fig. 3 result from the superposition of E_1 and E_2. Since the following experiments have been performed slightly below the ablation threshold fluence, a new area of the sample surface has to be irradiated and imaged after every partial measurement of $R_{\mathrm{i}}(x, y, t)$ and $R_0(x, y)$. Therefore, the sample is positioned by an automated $x - y$ translation stage.

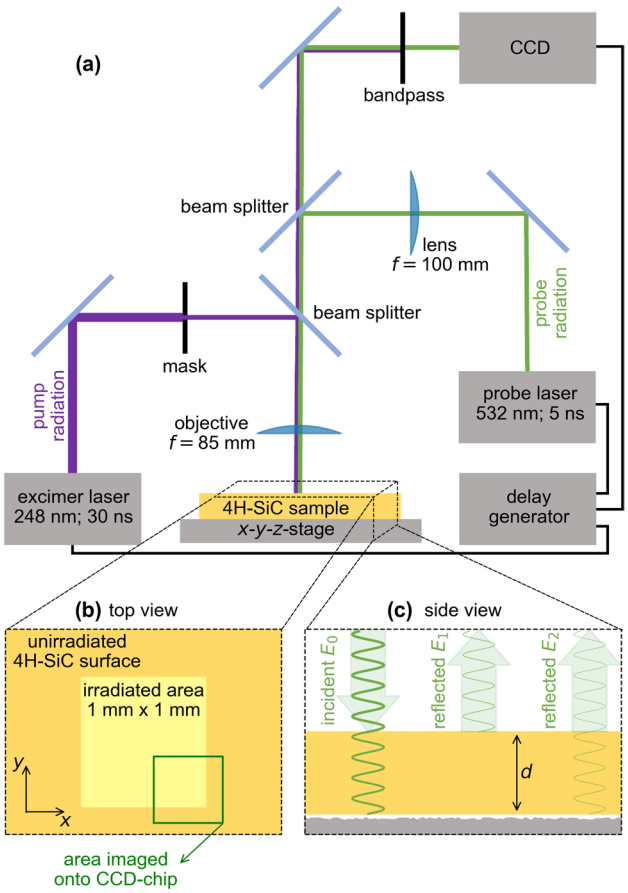

Fig. 2 **a** Scheme of the experimental pump-probe setup. **b** Schematic top view of the sample surface with the area excited by pump radiation (light yellow) and the area imaged onto the CCD chip (green square). **c** Schematic side view of the sample demonstrating its thickness d = 350 µm and the electric field strengths of the incident probe radiation E_0 and the partially reflected probe radiation E_1 and E_2

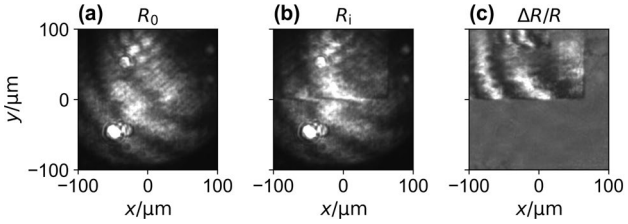

Fig. 3 Example of the relative change of reflectance $\Delta R/R$ (**c**) of the sample calculated from the signals detected on the CCD chip before (R_0, (**a**)), and after irradiation with pump radiation (R_{i}, (**b**))

3 Results and discussion

3.1 Surface modification

The SiC sample has been irradiated by mask-projected laser radiation with the wavelength λ_{pump}= 248 nm, the pulse duration $\tau_{H,pump}$= 30 ns, and the fluence H_0= 1.4 J/cm^2. As demonstrated in Fig. 2b, the irradiated area was A_{mask}= 10^{-6} m^2.

Similar to recently published studies [7, 8], a phase separation of the initial 4 H-SiC into three distinct layers was observed by TEM (Fig. 4). According to literature, the separated phases consist of regrown SiC with layers of silicon and carbon on top [7, 8] (Fig. 4). While the TEM measurement in Fig. 4 reveals the distinct layers, a more comprehensive characterization of the atomic order would require HR-TEM investigations. However, according to literature, the regrown SiC layer is expected to exhibit a composite structure of 3C-SiC and 6 H-SiC grains, with crystalline silicon and partially graphitic carbon on top [7, 8]. The phase separation of the SiC sample after irradiation is accompanied by an increased reflectance of the sample surface with a relative change of $\Delta R/R \approx 0.1$, whereas the sample surface topography has not been modified (Fig. 5a).

As a comparable experiment, the SiC sample was also irradiated by focused laser radiation with the wavelength

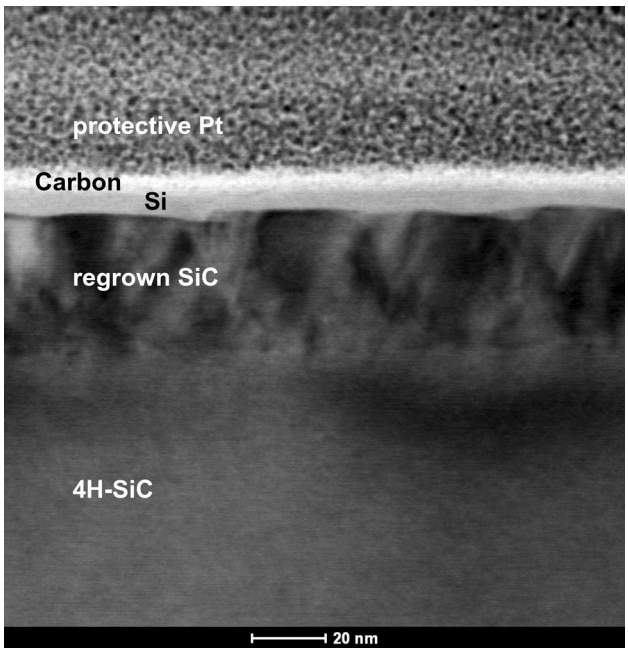

Fig. 4 TEM image of the phase separated area of the 4 H-SiC sample after irradiation with pump laser radiation (248 nm, 30 ns, 1.4 J/cm^2). The cross-section of the phase separated area was generated by FIB cleaving (see Sect. 2.1)

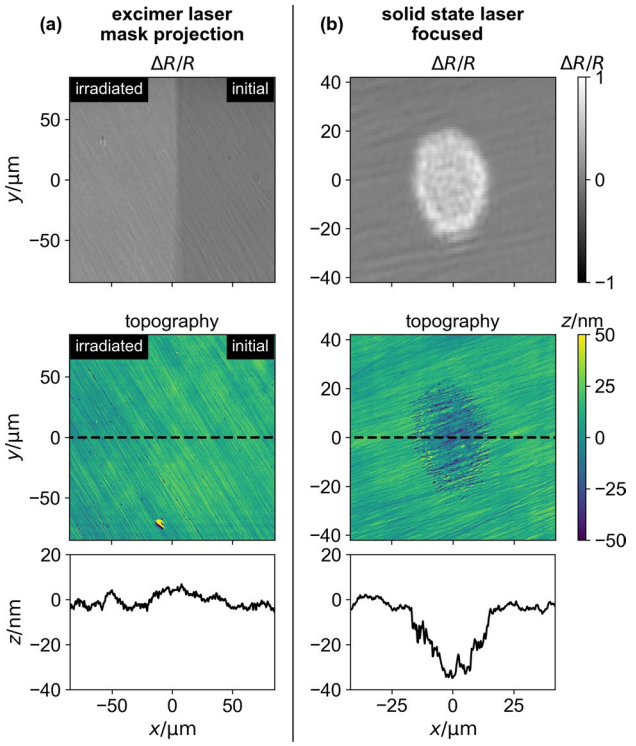

Fig. 5 $\Delta R/R$ and topography of the SiC sample after irradiation with mask-projected excimer laser radiation (**a** 248 nm, 30 ns, 1.4 J/cm^2) and focused laser radiation from a solid state laser (**b** 355 nm, 2.7 ns, 2 J/cm^2) detected by imaging ellipsometry (top: $\Delta R/R$) and laser scanning microscopy (bottom: topography)

λ_{pump}= 355 nm, the pulse duration $\tau_{H,pump}$= 2.7 ns, and the fluence H_0= 2.0 J/cm^2, as explained in Sect. 2.2. This time, the laser radiation was focused onto the SiC surface by a focusing lens with a focal length of 150 mm resulting in a beam radius of $w_{86} \approx 17$ µm. In contrast to the irradiation with excimer laser radiation, a change of reflectance is always accompanied by a modification of the sample surface. Due to ablation, the sample surface topography has been changed with a maximum ablation depth of approximately 35 nm. Thus, no phase separation without damaging the sample surface is feasible by using the focused laser radiation.

3.2 Transient reflectance

Time-resolved imaging pump-probe reflectometry has been applied to measure the relative change of reflectance $\Delta R/R$ of the SiC sample in the nanosecond to millisecond temporal range after irradiation with excimer laser pump radiation. The pump radiation features again a wavelength of 248 nm and a pulse duration of 30 ns, whereas the probe radiation has a wavelength of 532 nm with a pulse duration of 5 ns. The applied fluence of the pump radiation H_0= 1.4 J/cm^2 was below the damage threshold fluence, as no

modification of the sample surface topography has been detected after irradiation (see Fig. 5a). In the following, the signal detected on the CCD chip after excitation R_i and the resulting calculated relative change of reflectance $\Delta R/R$ of the SiC sample at different times after irradiation with pump radiation are described separately (Fig. 6). At the time t= 0, the maxima of the temporal intensity distributions of the pump and the probe radiation interact with the sample surface, which was measured by a Si-photodiode and an oscilloscope with an accuracy of ± 10 ns.

Before irradiation, at $t < 0$ in Fig. 6a, the measured spatially resolved R_i features interference patterns resulting from the probe radiation being partially reflected on the top and bottom interface of the the SiC sample (see Fig. 2c). At $t = 0$ µs, the interference patterns at $y > 0$ are shifted relatively to those at $y \leq 0$, resulting in a sharp edge at $y = 0$ (Fig. 6a). This sharp edge becomes increasingly blurred at $t > 0$ until no phase shift is visible anymore at $t \geq 12$ µs. In contrast to previous studies [7, 14], no significant increase in R_i upon irradiation has been detected. As the surface has not been modified after the irradiation, the transient phase shift observed in $R_i(t \geq 0)$ necessarily results from a changed optical path length $l_{opt} = n \cdot d$ of the probe radiation being reflected on the rear side of the sample (see E_2 in Fig. 2). A clear distinction on whether a changing thickness d or a changing refractive index n of the sample induce the increased optical path length is not possible by considering the measured R_i only. However, both properties are most certainly affected by the thermal expansion of the sample due to heating or by the onset of the laser induced phase changes [19], that have been observed by TEM (Fig. 4).

By considering the resulting $\Delta R/R$, the sharply defined area of the sample with a changed optical path length $l_{opt} = n \cdot d$ at $y > 0$ and $t \geq 0$ becomes visible even more clearly (Fig. 6b). Therefore it should be emphasized again, the change in $\Delta R/R$ at $y > 0$ and $t \geq 0$ results not from a changed reflectance of the sample surface, but from a phase shift of the probe radiation being reflected on the rear side of the sample. This sharp edge between the area with a changed $\Delta R/R$ and the surrounding non-irradiated

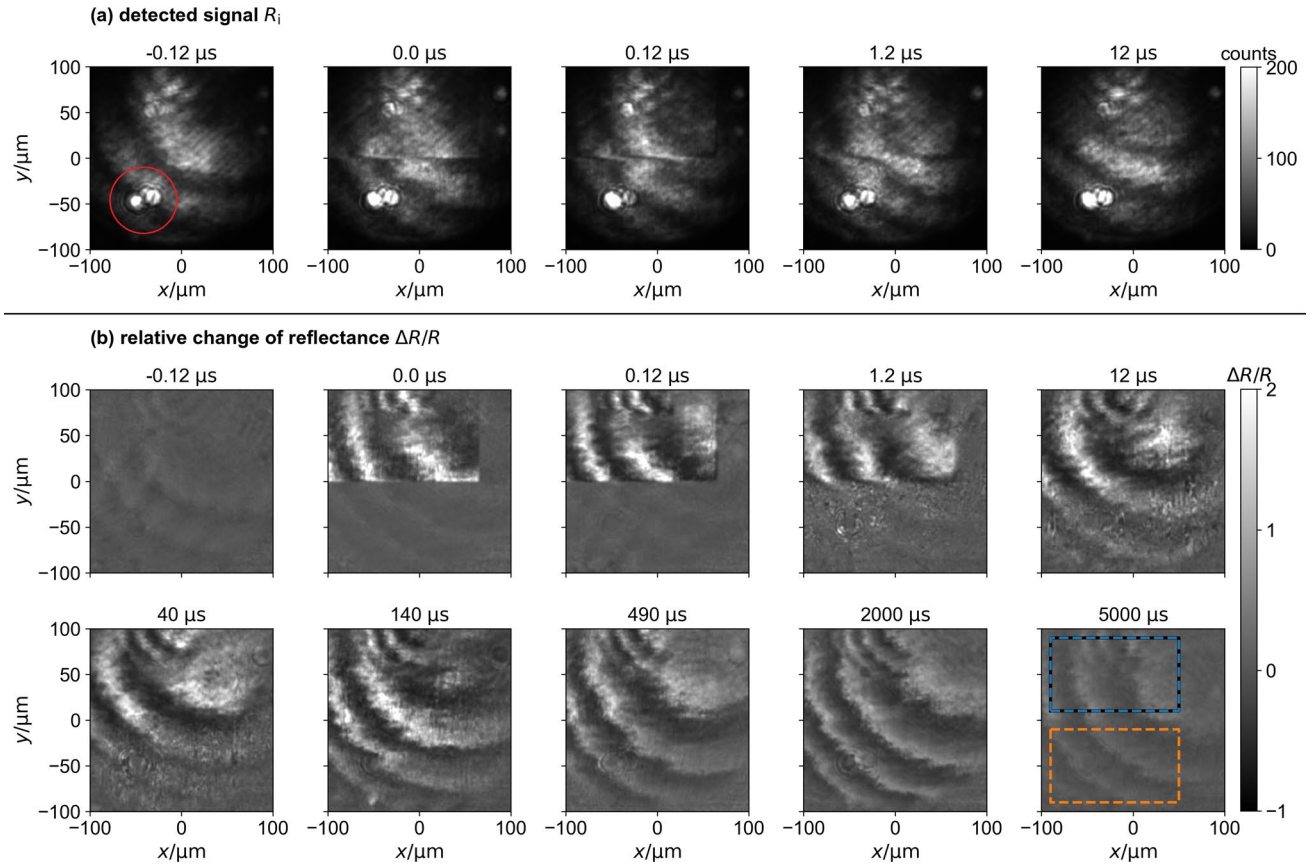

Fig. 6 Signal R_i detected with the CCD chip (**a**) and the calculated relative change of reflectance $\Delta R/R$ (**b**) of the SiC sample measured by pump-probe reflectometry at different times after irradiation with pump radiation (248 nm, 30 ns). The bright spots visible in the measured R_i (red circle) result from a reflection of the probe radiation on the objective, and is independent of the excitation dynamics of the SiC sample. The blue and orange squared dashed areas correspond to the regions from which the difference $\Delta(\Delta R/R) = \max(\Delta R/R) - \min(\Delta R/R)$ in Fig. 7 is calculated

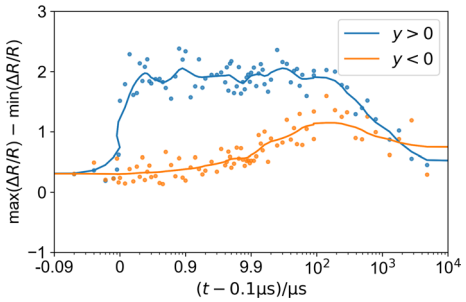

Fig. 7 Temporal evolution of the difference $\Delta(\Delta R/R) = \max(\Delta R/R) - \min(\Delta R/R)$ calculated from the measured spatially resolved $\Delta R/R$ for $y > 0$ and $y < 0$ as demonstrated by the dashed areas in Fig. 6. The logarithmic scaled abscissa has been shifted by 0.1 µs

area gets increasingly blurred for longer times. This broadening of the area with a changed $\Delta R/R$ most certainly results from heat conduction from the irradiated into the non-irradiated area, and is detectable up to a few milliseconds after irradiation.

To quantify the temporal evolution of the heat conduction into the non-irradiated area, the difference $\Delta(\Delta R/R) = \max(\Delta R/R) - \min(\Delta R/R)$ has been calculated for both areas $y > 0$ and $y < 0$, respectively (Fig. 7). For $y > 0$, $\Delta(\Delta R/R)$ increases abruptly after irradiation, remains approximately constant until 100 µ s, and decreases afterwards. For $y < 0$, $\Delta(\Delta R/R)$ increases much slower until 100 µs. By assuming that the changed $\Delta R/R$ results from a changed optical path length $l_{\mathrm{opt}} = n \cdot d$ and the broadening of $\Delta R/R$ is caused by thermal heat conduction into the non-irradiated area, Fig. 7 indicates that the maximum temperature within the area $y < 0$ is reached at $t \approx 100$ µs. Afterwards, further heat conduction leads to cooling accompanied by a steady decrease of $\Delta(\Delta R/R)$.

3.3 Temperature evolution

The two-dimensional heat conduction in SiC has been calculated by applying the numerical finite difference method for solving the two-dimensional heat equation

$$\rho\, c\, \frac{\partial T}{\partial t} = L_{\mathrm{th}}\, \Delta T + (1 - R(\lambda))\frac{\partial I}{\partial z} \quad . \tag{2}$$

The simulated area has been set to $350 \times 350\ \mu\mathrm{m}^2$, with 2^9 elements for each dimension. The thermophysical properties of the SiC sample are assumed to be constant with the density $\rho = 3210\ \mathrm{kg/m^3}$, the specific heat capacity $c = 690$ J/kg/K, and the thermal conductivity $L_{\mathrm{th}} = 370$ W/m/K [20]. The spatial and temporal intensity distribution of the exciting laser radiation is given by

$$I(x, z, t) = I(x)\, e^{\left(-4\ \ln(2)\ \frac{t^2}{\tau^2_{\mathrm{H,pump}}}\right)}\, e^{(-\alpha z)}\,, \tag{3}$$

with absorption coefficient α and the spatial intensity distribution $I(x)$ of the corresponding pump radiation from Fig. 1. For the excimer laser radiation, an absorption coefficient of $\alpha(248\ \mathrm{nm}) = 9.2 \cdot 10^5\ \mathrm{cm}^{-1}$ is assumed resulting from equation $\alpha = 4\pi k/\lambda_{\mathrm{pump}}$ using the complex refractive index $\tilde{n}(248\ \mathrm{nm}) = n - \mathrm{i}k = 3.26 - 1.82\mathrm{i}$ tabulated in the literature [21]. For the focused laser radiation, the considered absorption coefficient is $\alpha(355\ \mathrm{nm}) = 210\ \mathrm{cm}^{-1}$ [22]. The optical penetration depth $d_z = 1/\alpha$ results to approximately $d_z(248\ \mathrm{nm}) = 10$ nm for the excimer laser radiation, and $d_z(355\ \mathrm{nm}) = 48$ µm for the focused laser radiation. Melting is not considered in this first order approximation.

In the case of the mask-projected excimer laser irradiation (Fig. 8 a, 248 nm, 30 ns, 1.4 J/cm^2), the whole simulated area – 175 µm $\leq x \leq$ 175 µm near the surface is heated to a maximum temperature of approximately 3100 K directly upon irradiation. Due to the broad lateral dimension of the heated area, the subsequent heat conduction is predominantly directed to one dimension along the z-coordinate. On the contrary, the focused laser irradiation (Fig. 8b, 355 nm, 2.7 ns, 2.0 J/cm^2) heats the smaller area – 20 µm $\leq x \leq$ 20 µm. Due to the much larger optical penetration depth, the calculated maximum temperature of approximately 500 K is much smaller directly after irradiation. Additionally,

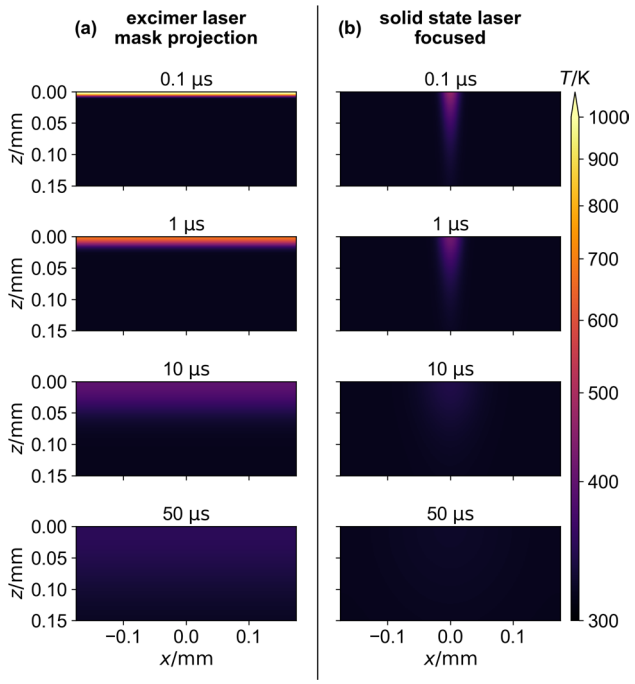

Fig. 8 Spatial temperature distribution in SiC at different times after irradiation with mask-projected excimer laser radiation (**a** 248 nm, 1.4 J/cm^2) and focused laser radiation (**b** 355 nm, 2.0 J/cm^2)

the much larger penetration depth coupled with the smaller lateral dimension of the heated area leads to heat conduction into both dimensions x and z, and thus a larger cooling rate in comparison to the excimer laser irradiation. Considering these temperature calculations only, no unambiguous conclusions can be derived about the mechanisms leading to ablation after focused laser irradiation. However, exploring such mechanisms is beyond the scope of this study and will not be further addressed.

4 Conclusion

A 1 mm^2 area of a 4 H-SiC wafer has been irradiated by mask-projected excimer laser radiation with the fluence $H_0 = 1.4$ J/cm^2, the wavelength $\lambda_{pump} = 248$ nm, and the pulse duration $\tau_{H,pump} = 30$ ns. This approach successfully replicated the laser-induced phase separation comparable to studies reported previously [7, 8] without damaging the sample surface. The resulting structural phase change of the pristine 4 H-SiC into separated C and Si layers on top of a regrown SiC layer after melting was confirmed by TEM analysis. Despite the absence of observable surface modifications, imaging ellipsometry revealed a change in the optical properties within the phase-separated area. In contrast to the excimer laser irradiation, focused laser irradiation of a 4 H-SiC wafer area three orders of magnitude smaller ($w_{86} \approx$ 17 µm, 355 nm, 2.7 ns, 2.0 J/cm^2) could not induce phase separation without damaging the sample surface.

In order to get a deeper understanding of the physical processes, in particular heating and subsequent cooling, during the laser-induced phase separation, time-resolved pump-probe reflectometry upon excimer laser irradiation has been coupled with complementary numerical simulations of the resulting temperature gradient. The applied probe radiation with the wavelength λ_{probe}= 532 nm and the pulse duration $\tau_{H,probe}$= 5 ns was synchronized relatively to the excimer laser radiation by an external delay generator resulting in a temporal resolution of Δt= 5 ns being limited by $\tau_{H,probe}$. In contrast to former studies [7, 14], the reflectance of the sample surface did not increase abruptly after the excimer laser irradiation. Nonetheless, a relative change of reflectance $\Delta R/R$ could still be detected, which is attributed to a phase shift of the interfering probe radiation being partially reflected on the front and the rear side of the sample. This phase shift corresponds to a changed optical thickness of the sample due to laser heating. Subsequent heat conduction after the laser irradiation led to a lateral expansion of the area with changed $\Delta R/R$, which remained measurable for several milliseconds. The numerical simulations of the temporal temperature evolution upon mask-projected irradiation reveal that the laser energy is absorbed within a few nanometers near the sample surface resulting in a maximum temperature of 3100 K being similar to the melting temperature of 4 H-SiC. Additionally, the simulations demonstrate a predominant one-dimensional heat conduction into depth due to the broad lateral dimension of the irradiated area. Consequently, the laser energy being distributed across a broad area near the sample surface coupled with the constrained one-dimensional heat conduction results in sustained higher temperatures over an extended period of time after the mask-projected excimer laser irradiation. This sustained high temperature and the accompanied sustained heat conduction correlate with the relative change of reflectance being observable up to the millisecond range in Fig. 6. Furthermore, the pulse duration of the excimer laser radiation, which is 10 times longer than for the focused solid state laser radiation, contributes to a slower heating rate. This combination of gradual heating and cooling of the sample surface might abet the observed phase separation demonstrated in Fig. 3, which was absent in the case of focused laser irradiation (Fig. 5). The contrasting effects between mask-projected excimer laser irradiation and focused solid state laser irradiation can most probably be attributed to the differences in irradiated area size and optical penetration depth. Focused laser irradiation featured a much smaller lateral dimension of the irradiated area and a much larger optical penetration depth, resulting in a lower peak temperature and much faster cooling, both being less conducive for inducing phase separation.

In summary, this study unveils that the feasibility of laser-induced phase separation in 4 H-SiC highly depends on the degrees of freedom of the heat conduction from the irradiated to non-irradiated areas and the optical penetration depth. This dependencies indicate that the feasibility of laser-induced phase separation can be tailored by adjusting the properties of the exciting laser radiation in terms of beam dimension, pulse duration, wavelength, and repetition rate. Furthermore, the introduced imaging pump-probe reflectometer represents a suitable tool for investigating the transient dynamics and refining the laser-induced phase separation in future research.

Acknowledgements T.P. and A.H. gratefully thank the German Research Foundation (DFG) for funding the project no. 469106482, and the Federal Ministry for Economic Affairs and Energy for funding the project 03EE1125B.

Author contributions Conceptualization: TP, BB, AH; Methodology: TP, BB, FJ; Formal analysis and investigation: TP, BB; Writing—original draft preparation: TP; Funding acquisition: AH; Resources: SW, AH; Supervision: MG, SW, AH

Funding Open Access funding enabled and organized by Projekt DEAL.

Data availability The data presented in this study are available on request from the corresponding author.

Declarations

Conflict of interest The authors declare no Conflict of interest.

References

1. C. Yun et al., Generating semi-metallic conductivity in polymers by laser-driven nanostructural reorganization. Mater. Horiz. **6**, 2143–2151 (2019)
2. T. Pflug et al., Spatial conductivity distribution in thin pedot:pss films after laser microannealing. ACS Appl. Electron. Mater. **3**, 2825–2831 (2021)
3. C. Florian et al., Single femtosecond laser-pulse-induced superficial amorphization and re-crystallization of silicon. Materials (Basel, Switzerland) **14**, 90 (2021)
4. A. V. Agashkov, et al., Laser annealing of thin organic films. LAT 2010: International Conference on Lasers, Applications, and Technologies. SPIE Proceedings, 79940S, (2010)
5. P. Baeri, E. Rimini, Laser annealing of silicon. Mater. Chem. Phys. **46**, 169–177 (1996)
6. T. Pflug et al., Laser-induced positional and chemical lattice reordering generating ferromagnetism. Adv. Function. Mater. 2311951 (2023)
7. I. Choi et al., Laser-induced phase separation of silicon carbide. Nat. Commun. **7**, 13562 (2016)
8. M. Vivona et al., Effects of excimer laser irradiation on the morphological, structural, and electrical properties of aluminum-implanted silicon carbide (4H-SiC). ACS Appl. Electron. Mater. **4**, 4514–4520 (2022)
9. Y. Wu et al., Formation of Ohmic contacts on laser irradiated n-type 6H-SiC without thermal annealing. Curr. Appl. Phys. **19**, 521–527 (2019)
10. T. Pflug et al., Case study on the dynamics of ultrafast laser heating and ablation of gold thin films by ultrafast pump-probe reflectometry and ellipsometry. Appl. Phys. A **124**, 116 (2018)
11. T. Pflug et al., Electron dynamics in fused silica after strong field laser excitation detected by spectroscopic imaging pump-probe ellipsometry. Phys. Rev. B **106**, 014307 (2022)
12. M. Olbrich et al., Hydrodynamic modeling and time-resolved imaging reflectometry of the ultrafast laser-induced ablation of a thin gold film. Opt. Lasers Eng. **129**, 106067 (2020)
13. P.-H. Wu et al., Real time monitoring of fs laser annealing on indium tin oxide. Opt. Laser Technol. **111**, 380–386 (2019)
14. D. Satoh et al., Ultrafast pump-probe microscopic imaging of femtosecond laser-induced melting and ablation in single-crystalline silicon carbide. Appl. Phys. A **126** (2020)
15. T. Pflug et al., Investigations on the modification of PMMA by ultrafast laser radiation from the UV to the mid-IR spectral range. Opt. Lasers Eng. **111**, 130–134 (2018)
16. T. Pflug et al., Fluence-dependent transient reflectance of stainless steel investigated by ultrafast imaging pump-probe reflectometry. J. Phys. Chem. C **125**, 17363–17371 (2021)
17. F.L. Pedrotti et al., *Introduction to Optics*, 3rd edn. (Pearson Addison Wesley, San Francisco, 2007)
18. S. Wang et al., 4H-SiC: a new nonlinear material for midinfrared lasers. Laser Photon. Rev. **7**, 831–838 (2013)
19. E. Hecht, *Optics*, 5th edn. (Pearson, Boston, 2017)
20. M.E. Levinshtein et al., *Properties of Semiconductor Materials: GaN, AIN, InN, BN, SiC, SiGe* (John Wiley & Sons, New York, 2001)
21. J.I. Larruquert et al., Self-consistent optical constants of SiC thin films. J. Opt. Soc. Am. A **28**, 2340–2345 (2011)
22. S. Sridhara et al., Penetration depths in the ultraviolet for 4H, 6H and 3C silicon carbide at seven common laser pumping wavelengths. Mater. Sci. Eng. B **61**, 229–233 (1999)